The Astrophysical Journal, 741:120 (10pp), 2011 November 10 doi:10.1088/0004-637X/741/2/120

HOT MOLECULAR CORES IN INFRARED DARK CLOUDS

J. M. Rathborne[1,5], G. Garay[1], J. M. Jackson[2], S. Longmore[3], Q. Zhang[3], and R. Simon[4]
[1] Departamento de Astronomía, Universidad de Chile, Casilla 36-D, Santiago, Chile; rathborn@das.uchile.cl, guido@das.uchile.cl
[2] Institute for Astrophysical Research, Boston University, Boston, MA 02215, USA; jackson@bu.edu
[3] Harvard-Smithsonian Center for Astrophysics, Mail Stop 42, 60 Garden Street, Cambridge, MA 02138, USA; slongmore@cfa.harvard.edu, qzhang@cfa.harvard.edu
[4] I.Physikalisches Institut, Universität zu Köln, 50937 Köln, Germany; simonr@ph1.uni-koeln.de
Received 2011 April 7; accepted 2011 August 4; published 2011 October 25

ABSTRACT

We present high angular resolution continuum images and molecular line spectra obtained at 345 GHz with the Submillimeter Array (SMA) toward two massive cores that lie within Infrared Dark Clouds (IRDCs): G034.43+00.24 MM1 and G024.33+00.11 MM1. Both of these cores contain bright, unresolved (<2″) objects that have previously been imaged in the millimeter/submillimeter continuum with the Institut de RadioAstronomie Millimétrique (IRAM) Plateau de Bure Interferometer and SMA and show complex molecular line chemistry. The new, higher angular resolution SMA continuum images reveal that both cores contain massive (8, 26 $M_{\odot}$), unresolved (0.″6; ∼3000 AU) continuum emission features and emission from many complex molecular transitions, which confirm that these are hot molecular cores, an early stage in the formation of a high-mass star. Because these hot cores are located within IRDCs, they may well represent the very earliest phases in the formation of high-mass protostars and, hence, their detailed study may reveal the initial conditions within high-mass star-forming cores, before they are shredded apart by stellar winds and radiation.

Key words: dust, extinction – radio lines: ISM – stars: formation – submillimeter: ISM

1. INTRODUCTION

Due to their relatively short lifetimes and the fact that they form within very dense, obscuring environments, the earliest phases of high-mass ($M > 8\,M_{\odot}$) star formation are difficult to identify. Because high-mass stars begin hydrogen burning and reach the pre-main-sequence before they emerge from their natal molecular core, their presence is often inferred from their effect on the surrounding molecular material. Hot molecular cores (HMCs), ultra-compact H II (UC H II) regions, masers, and outflows are all signposts of the earliest phases of high-mass star formation, as the strong stellar winds and intense UV radiation from the young star interact with the surrounding dense dust and gas.

One of the earliest and well-characterized phases associated with the early stage of high-mass star formation are the HMCs (Garay & Lizano 1999; Kurtz et al. 2000; Churchwell 2002). HMCs correspond to the compact (<0.1 pc), dense (∼10^5–10^8 cm^{-3}), and massive (∼$10^2\,M_{\odot}$; Garay & Lizano 1999; Kurtz et al. 2000; Churchwell 2002) molecular material that is heated in the immediate vicinity of the recently formed high-mass protostar. Because the environment is heated by the UV radiation from the high-mass star, HMCs display a complex chemistry and are characterized by a rich molecular line spectrum, which is dominated by emission from many complex molecules (e.g., Kurtz et al. 2000). Moreover, due to the internal heating from the central high-mass protostar, they are also typically very luminous (>$10^4\,L_{\odot}$). While the majority of HMCs contain an embedded high-mass star that is providing the central powering source, some HMCs appear not to be internally heated (e.g., Mookerjea et al. 2007). These are typically found in close proximity to H II regions and are thought to be externally heated by the radiation field from the nearby high-mass stars.

Because most HMCs trace the immediate environment surrounding a high-mass star that has already formed, HMCs correspond to a stage in the sequence of high-mass star formation after the central star has formed and well after the very earliest cold, dense starless core phase. While some HMCs are associated with UC H II regions, many have little or no observable radio continuum emission (Kurtz et al. 2000). As a result, HMCs are thought to be the precursors to UC H II regions and, thus, good signposts for an early phase of high-mass star formation. Masers and outflows have also been observed during the later HMC phase, which suggests that these HMCs may contain accretion disks (Kurtz et al. 2000; Beuther et al. 2002; Zhang et al. 2001, 2005; Zhang 2005; Cesaroni et al. 2007).

Many HMCs have been identified within regions of high-mass star formation, including two within infrared dark clouds (IRDCs; Rathborne et al. 2007, 2008). Because IRDCs are thought to harbor the very earliest stages of high-mass star and cluster formation (Rathborne et al. 2006), these HMCs may represent a very early phase in the hot core stage. Identified as extinction features against the bright Galactic mid-IR background, IRDCs are molecular structures that have very high column densities (∼10^{23}–10^{25} cm^{-2}) and very low temperatures (<25 K; Egan et al. 1998; Carey et al. 1998, 2000). They are the densest structures in much larger giant molecular clouds (Simon et al. 2006) and are currently undergoing the process of fragmentation and condensation, as evidenced by the many cold, dense, compact cores identified within them (Lis & Carlstrom 1994; Carey et al. 2000; Garay et al. 2004; Ormel et al. 2005; Beuther et al. 2005; Rathborne et al. 2005, 2006). Because the majority of these cores show no evidence for active star formation (e.g., Chambers et al. 2009; Rathborne et al. 2010), many of them are good candidates for the very earliest starless core phase of high-mass star formation. The remaining cores that do show evidence for current, active star formation are associated with bright 24 μm emission, broad molecular line emission, shocked gas, and maser emission (Chambers et al. 2009). Many of the

[5] Current address: CSIRO Astronomy and Space Science, P.O. Box 76, Epping NSW 1710, Australia.

Table 1
Core Properties

Core	Coordinates		V_{LSR}[a]	D[a]	Peak Flux	Deconvoled Diameter	Mass	L[b]	Σ
	R.A. (J2000)	Decl. (J2000)	(km s^{-1})	(kpc)	(mJy)	(pc)	($M_\odot$)	($L_\odot$)	(g cm^{-2})
G034.43+00.24 MM1	18:53:18.01	1:25:25.5	57.1	3.7	748	0.0105	8	$10^{4.4}$	19
G024.33+00.11 MM1	18:35:08.14	−7:35:04.1	113.4	6.3	843	0.0112	26	$10^{4.7}$	56

Notes.
[a] From Rathborne et al. (2006, 2007).
[b] From the gray-body fit to the SEDs presented within Rathborne et al. (2010). We assume that all of the observed bolometric luminosity arises from the single, high-mass object.

most massive and luminous of these cores are thought to harbor high-mass protostars (Beuther et al. 2005; Rathborne et al. 2005, 2010; Pillai et al. 2006; Wang et al. 2006).

Because of its short evolutionary timescale, high-mass star formation remains poorly understood. Since they are so young, IRDCs provide an excellent opportunity to study high-mass protostars in their very earliest phases. Because IRDCs are typically at distances of ∼4 kpc, millimeter/submillimeter interferometric observations are critical to probe their internal structure. Indeed, our recent Institut de RadioAstronomie Millimétrique (IRAM) Plateau de Bure Interferometer 1.3 mm (Rathborne et al. 2007) and SMA 345 GHz (Rathborne et al. 2008) observations toward two high-mass IRDC cores that show evidence for star formation, revealed very rich molecular spectra from a compact ($\lesssim$0.04 pc; 8,000 AU) region. These IRDC cores, G034.43+00.24 MM1 and G024.33+00.11 MM1, likely contain very young HMCs.

Our previous interferometric data also show circumstellar structure: toward G034.43+00.24 MM1 we see extended ^{13}CO (3–2) emission with a large velocity gradient (Rathborne et al. 2008). This emission appears to be tracing a large rotating structure. Moreover, both single-dish and interferometric CO and SiO observations show evidence for a powerful and energetic outflow perpendicular to this rotation (Shepherd et al. 2007; Q. Zhang 2010, private communication; Sanhueza et al. 2010). Evidence for disks around high-mass protostars exists for only a few objects (Garay & Lizano 1999; Zhang 2005; Cesaroni et al. 2007). Thus, the existence of circumstellar disks associated with young hot cores will confirm that high-mass stars can form via accretion, in a similar way to low-mass stars, rather than via coalescence. Because hot cores in IRDCs are very young, they are the best candidates to search for high-mass accretion disks given their short lifetimes.

In this paper we present new observations obtained using the extended array configuration of the SMA. These data further probe the small-scale structure of the two high-mass protostellar cores: G034.43+00.24 MM1 and G024.33+00.11 MM1. Both of these cores show evidence for active, high-mass star formation: bright 24 μm point source, broad molecular line emission, shocked gas, water maser emission, molecular outflows, and HMC chemistry (Garay et al. 2004; Shepherd et al. 2004; Rathborne et al. 2005, 2006, 2007, 2008; Wang et al. 2006; Sanhueza et al. 2010). G034.43+00.24 MM1 also shows weak radio continuum emission consistent with a deeply embedded B2 protostar (Shepherd et al. 2004). We find that both cores contain a single, unresolved, bright, central source in the continuum images, while their molecular line spectra reveal many emission lines from complex molecules. Our results confirm that these cores indeed contain an HMC and are thus tracing the environment surrounding a recently formed high-mass star.

2. OBSERVATIONS AND DATA REDUCTION

Interferometric observations of G034.43+00.24 MM1 and G024.33+00.11 MM1 were carried out with the Submillimeter Array[6] (SMA; Ho et al. 2004) on 2007 September 3 with seven antennas in the extended configuration. The projected baselines of the visibility data range from 25 m to 220 m. The double-sideband receivers cover a total of 4 GHz bandwidth. The digital correlator was configured to cover 329.1–331.1 GHz for the lower sideband and 339.1–341.1 GHz for the upper sideband with a uniform channel spacing of 0.8125 MHz (∼0.7 km s^{-1}) across the entire band.

The 336 GHz zenith opacities, measured with the NRAO tipping radiometer located at the Caltech Submillimeter Observatory, were $\tau \sim 0.14$ (scaled from the 225 GHz measurement via $\tau_{336\,\mathrm{GHz}} = 2.8 \times \tau_{225\,\mathrm{GHz}}$). The measured double-sideband system temperatures corrected to the top of the atmosphere were between 150 and 400 K.

The primary beam of the SMA at these frequencies is ∼37″. The phase centers for the observations are listed in Table 1. We used the quasars 1751+096 and 1743−038 to calibrate time dependent gains, and 3C454.3 to remove the gain variations across the passband. The flux scale was referenced to Uranus. The visibility data were calibrated with the IDL superset MIR package developed for the Owens Valley Radio Observatory (OVRO) interferometer. The absolute flux level is accurate to about 25%. After the calibration in MIR, the visibility data were exported to the MIRIAD format for further processing and imaging. The continuum is constructed from the line-free channels in the visibility domain, and is further self-calibrated using the clean components of the image as input models. The gain solutions from the continuum self-calibration are then applied to the spectral line data. The rms noise in the naturally weighted maps is ∼35 mJy beam^{-1} in the continuum images and 200 mJy beam^{-1} per channel in the line data. The average of the major and minor axis of the final synthesized beam was ∼0.″6 which corresponds to a physical size of ∼0.011 pc (∼2300 AU) and ∼0.020 pc (∼4000 AU) for the assumed distances of 3.7 kpc for G034.43+00.24 MM1 and 6.3 kpc for G024.33+00.11 MM1, respectively.

3. RESULTS

Figure 1 shows the new SMA extended array 345 GHz continuum images toward the two IRDC cores. Coincident with the peak in lower angular resolution images (2″and 11″), we find that the continuum emission toward these cores arises from

[6] The Submillimeter Array is a joint project between the Smithsonian Astrophysical Observatory and the Academia Sinica Institute of Astronomy and Astrophysics, and is funded by the Smithsonian Institution and the Academia Sinica.

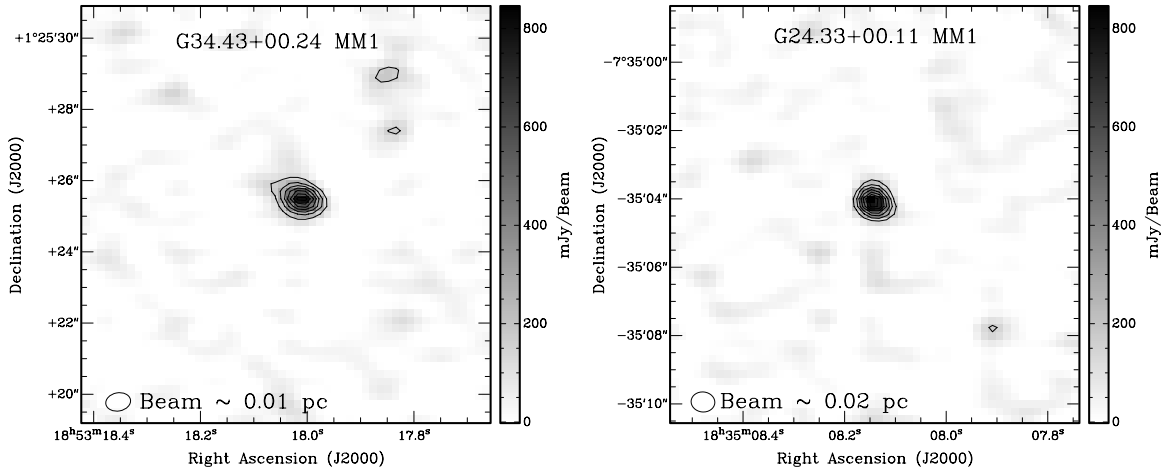

Figure 1. SMA 345 GHz continuum images toward the cores G034.43+00.24 MM1 (left panel) and G024.33+00.11 MM1 (right panel). The contour levels in both cases are 150–800 in steps of 100 mJy beam^{-1}. These cores were first identified in single-dish observations at 11″ angular resolution (the approximate extent of these images). We find that in these high angular resolution images both cores are dominated by a single, unresolved, massive emission feature. Table 1 lists their derived properties.

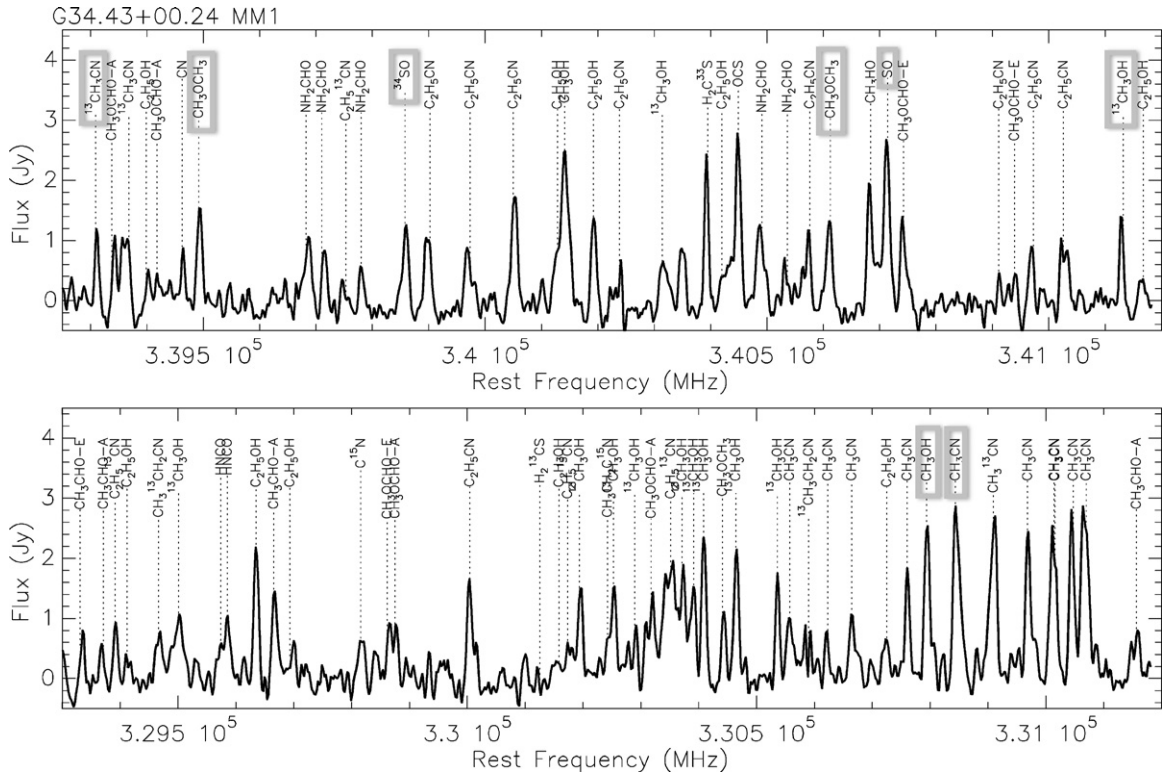

Figure 2. Spectrum toward G034.43+00.24 MM1. Both the lower and upper sidebands are shown (lower and upper panels, respectively). The spectrum is averaged over a ∼1.″2 region centered on the peak in the high-angular resolution continuum image. Note the strong emission from the many complex molecules, confirming that G034.43+00.24 MM1 is an HMC associated with the very earliest stage in the formation of a high-mass protostar. The expected frequencies for a selection of molecules within this range are plotted on the spectrum. The gray boxes mark the lines for which integrated intensity images and channel maps are shown in Figures 4 and 5 respectively.

a single, unresolved object (∼0.01 pc; ∼2000 AU). Compared to the previous interferometric images, we find that ∼30% of the continuum flux has been recovered in the new data, which is consistent with a centrally condensed emission feature and the increase in angular resolution. Table 1 lists the positions, deconvolved sizes, and peak fluxes which were determined from Gaussian fits to the emission.

Toward the peak of the continuum emission for both cores, we find that the spectra contain numerous emission lines from many complex nitrogen-, oxygen-, and sulfur-rich molecules and their isotopomers (Figures 2 and 3). Labeled on these spectra are the expected locations of the molecules CH_3CN, CH_3OH, CH_3OCH_3, CH_3OCHO, SO, SO_2, NH_2CHO, C_2H_5OH, C_2H_5CN, CN, NH_2CHO, H_2CS, OCS, and HNCO and their isotopomers. However, due to the large number of complex molecular transitions, many of the observed emission features may arise due to the blending of several individual species. Moreover, because of the large number of molecular transitions within this frequency range, this list of molecules is by no means complete. Without a detailed comparison to all

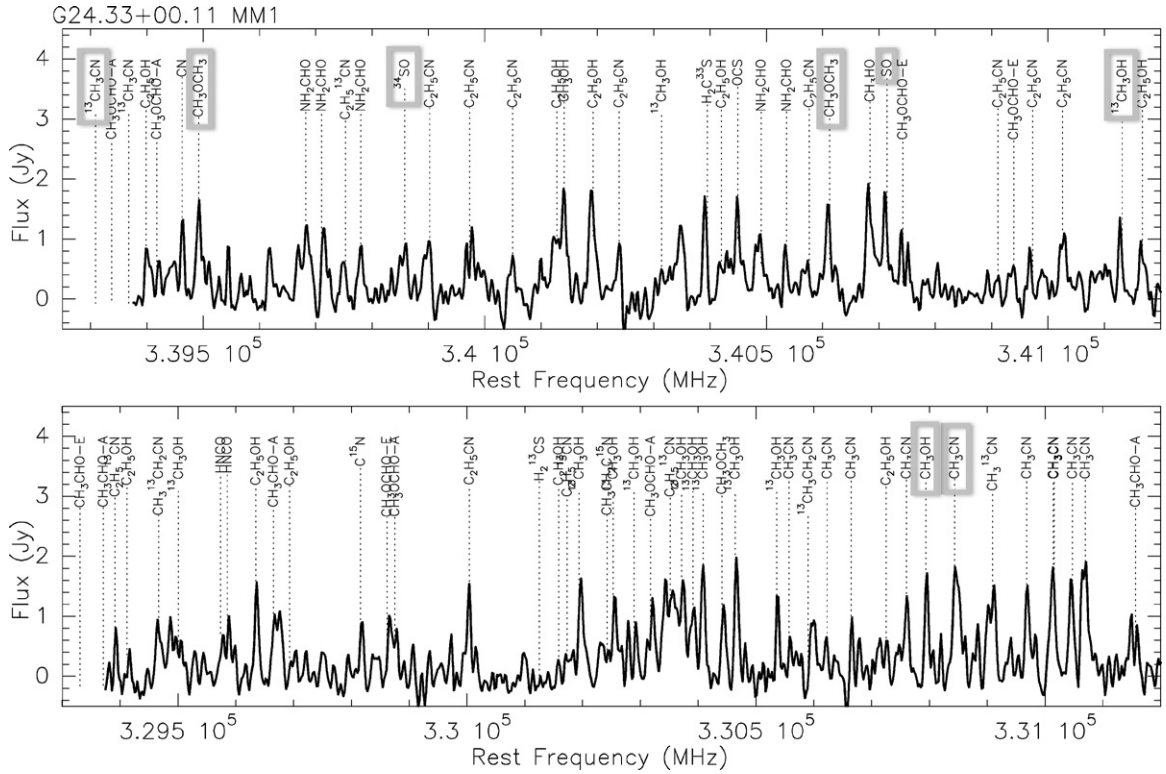

Figure 3. Spectrum toward G024.33+00.11 MM1. Both the lower and upper sidebands are shown (lower and upper panels, respectively). The spectrum is averaged over a ∼1.″2 region centered on the peak in the high angular resolution continuum image. Note the strong emission from the many complex molecules, confirming that G024.33+00.11 MM1 is an HMC associated with the very earliest stage in the formation of a high-mass protostar. The expected frequencies for a selection of molecules within this range are plotted on the spectrum. The gray boxes mark the lines for which integrated intensity images and channel maps are shown in Figures 7 and 8 respectively. Note that the spectrum is artificially truncated in the upper side band for frequencies <339.4 GHz.

(potentially) expected molecules a definitive line identification cannot be made. Thus, not all the molecules labeled on these plots may be proper identifications. Nevertheless, because many of these complex molecules are produced and excited in the immediate surroundings of a recently formed high-mass protostar as the grain ice mantles are evaporated (see Kurtz et al. 2000 and references therein), their detection over small spatial scales confirms the presence of HMCs within these cores.

In contrast to the single-dish (11″) and previous interferometric data (2″), the new spectra reveal very little CO emission. Both the ^{13}CO (3–2) and C^{18}O (3–2) transitions are within the band, but we observe no significant emission. The previous data reveal extended CO emission on spatial scales of >0.5 pc (>11″). Thus, the lack of CO emission in these data indicates that the CO emission is diffuse and extended and reflects the absence of short baselines in these data. The fact that CO is detected in the lower angular resolution images but is completely resolved out by the interferometer at the higher angular resolution suggests that CO is not associated with the dense core gas at the smallest scales.

4. DISCUSSION

4.1. CH_3CN: Excitation Temperatures and Column Densities

With the detection of such a rich molecular spectrum, one can use the combination of the molecular transitions to obtain estimates of the physical parameters of the gas. While we detected over 70 molecular transitions from more than 15 molecules and their isotopomers, we use the methyl cyanide (CH_3CN) emission as a tracer of the gas temperature and density. Because CH_3CN is a symmetric top molecule with a high dipole moment (3.913 Debye), it is particularly sensitive to regions of high density. Moreover, CH_3CN has a further advantage of having, for a given J rotational transition, several K quantum number transitions that can be observed simultaneously. Since the relative intensities of the K components directly measure collisions, it is closely related to the kinetic temperature (T_k) and density of the gas (Solomon et al. 1971). Thus, simultaneous observations of several K components from the same J level can provide an estimate of T_k and the total beam-average column density without being affected by calibration errors. In the high density limit and assuming local thermal equilibrium (LTE) conditions, $T_k \sim T_{\rm rot}$, the rotational temperature.

Within our spectra we see emission from the J = 18–17 rotational level and the K = 0, 1, 2, 3, 4, 5, 6, 7, and 8 components. We use the averaged spectrum at the peak of the submillimeter continuum shown in Figures 2 and 3 as input to the fitting routine. Using the code of Qiu & Zhang (2009), which assumes LTE conditions, the best-fit rotational temperature, column density, and beam filling factor are determined via a χ^2 minimization between a synthetic spectrum and the input data. For G034.43+00.24 MM1 the K = 0 and 1 components were severely blended, so the fits were generated using only the K = 2–8 components. Table 2 lists the values derived from these fits.

Because we have also observed G034.43+00.24 MM1, with this spectral setup of the SMA in the compact configuration (2″ angular resolution; Rathborne et al. 2008), we can use these additional data to also derive the gas parameters over the larger spatial region. These results are also listed in Table 2. As expected, the derived (beam averaged) CH_3CN temperature, column density, and filling factor (η) are lower in the data that

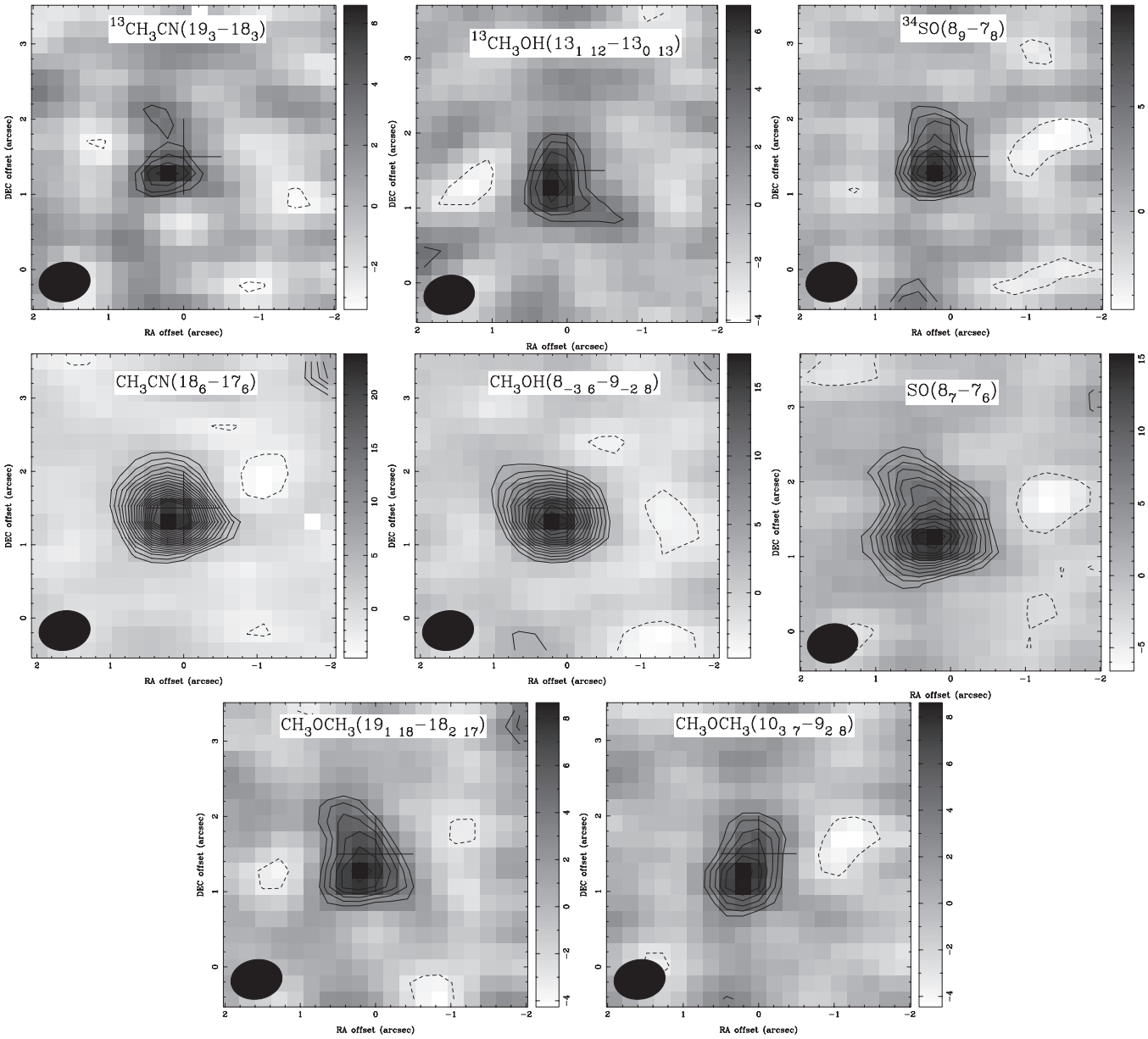

Figure 4. G034.43+00.24 MM1 integrated intensity images for a selection of the bright, unblended lines identified in Figure 2. In all cases the contour levels are -3σ, 3σ to 19σ in steps of 1σ, where σ is 1.0 K km s^{-1}. The cross marks the position of the peak pixel in the continuum emission. The axes on all images are labeled in arcseconds offset from the pointing center of the observations (R.A. 18:53:18.0, decl. +01:25:24, J2000), which was taken from the low-resolution (11″), single-dish continuum image.

Table 2
Results from the CH_3CN Fitting

Core	SMA	R (pc)	T_{rot} (K)	N(CH_3CN) (cm^{-2})	η^a
G034.43+00.24 MM1[b]	Compact	0.010	110	3×10^{16}	0.10
	Extended	0.005	210	1×10^{17}	0.50
G024.33+00.11 MM1	Extended	0.005	670	7×10^{17}	0.09

Notes.
[a] η is the beam filling factor.
[b] Due to significant blending, the fits for this source were generated by excluding the $K = 0$ and 1 components.

samples the larger spatial region (marked as SMA-compact in Table 2). The differences in these derived parameters are similar to other HMCs observed on comparable spatial resolutions (e.g., Olmi et al. 1996) and represent the values for the hotter, compact core and the cooler, more extended halo. This temperature gradient suggests central heating with a reasonable exponent, which is expected if the hot cores are internally heated by the recently formed high-mass star.

4.2. Masses and Luminosities

Using the peak fluxes measured from the 345 GHz continuum images and assuming that the emission is optically thin, we calculate the core gas masses using the expression

$$M = \frac{F_\nu D^2}{\kappa_\nu R B_\nu(T_D)}$$

(Hildebrand 1983), where F_ν is the observed source flux density, D is the distance, κ_ν is the dust opacity per gram of dust, and $B_\nu(T_D)$ is the Planck function at the dust temperature, T_D. In all cases, we assume that R, the gas-to-dust mass ratio,

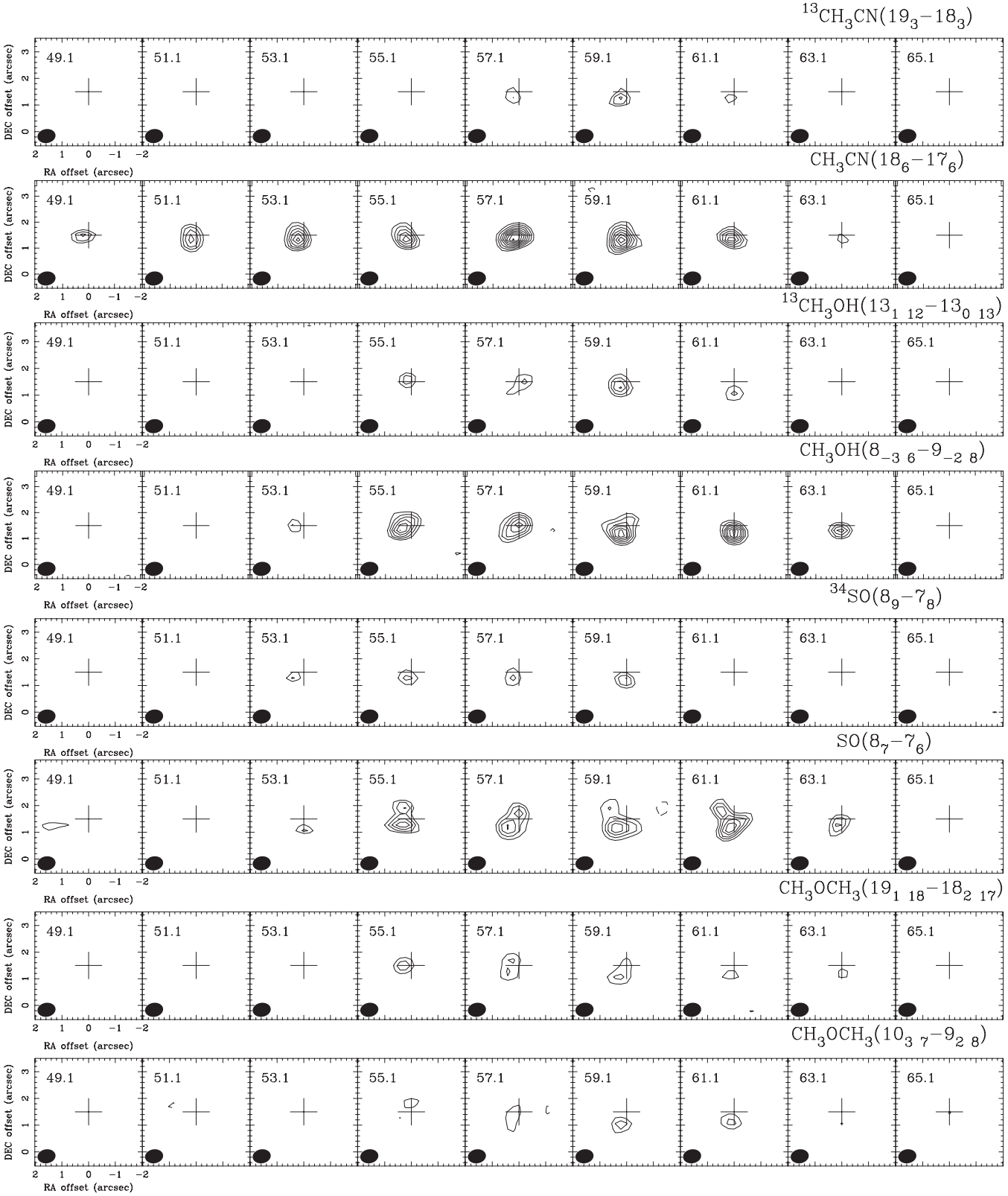

Figure 5. G034.43+00.24 MM1 channel maps of the bright, unblended lines shown in Figure 4. The V_{LSR} for this source is 57.1 km s^{-1}. In all cases the contour levels are -3σ, 3σ to 19σ in steps of 1σ, where σ is 0.17 Jy beam^{-1}. Note that the emission is extended and that an $\sim$5 km s^{-1} velocity gradient is apparent in the CH_3OH emission. The axes on all images are labeled in arcseconds offset from the pointing center of the observations (R.A. 18:53:18.0, Decl. +01:25:24, J2000), which was taken from the low-resolution (11″), single-dish continuum image.

is 100. We estimate $\kappa_{0.87\,mm}$ by scaling the value of $\kappa_{1.3\,mm}$ (1.0 cm^2 g^{-1}; Ossenkopf & Henning 1994) by ν^{β}, where β is the dust emissivity index.

We assume a value for T_D of 100 K and for β of 1.5. Modeling of the dust temperature as a function of radius from HMCs shows that this temperature is typical for a radius of

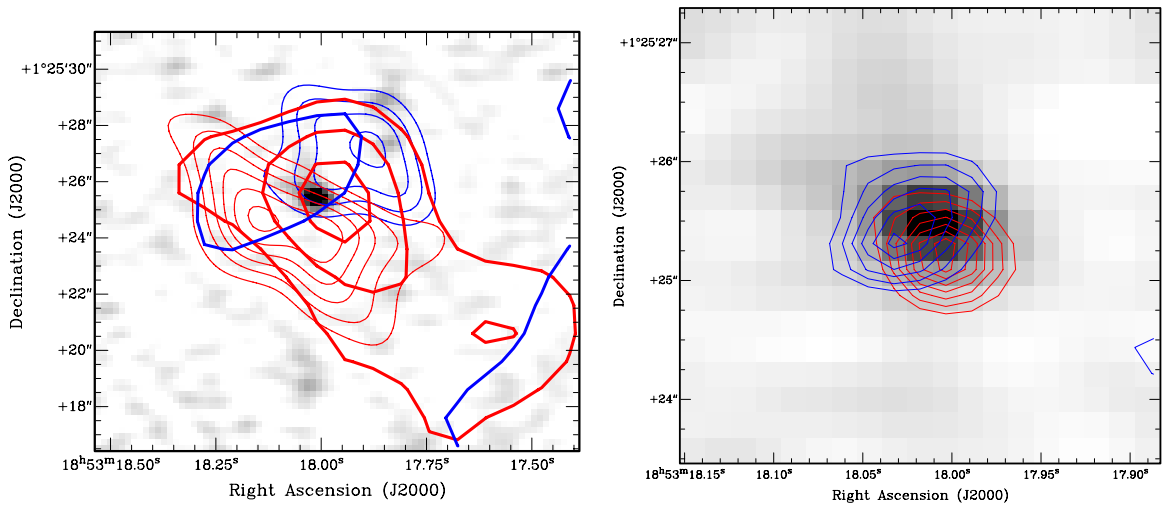

Figure 6. SMA 345 GHz continuum image toward the core G034.43+00.24 MM1 overlaid with left panel: ^{13}CO (1–0) emission (thick contours; red shifted emission is from 63.1 to 61.8 km s^{-1}, blueshifted emission is from 52.3 to 49.5 km s^{-1}, levels are 0.3, 0.6, 0.9 Jy beam^{-1}; Shepherd et al. 2007) and ^{13}CO (3–2) emission (thin contours; redshifted emission is at 61 km s^{-1}, blueshifted emission is at 55 km s^{-1}, levels are 1.7 to 6.7 in steps of 1.0 Jy beam^{-1}; Rathborne et al. 2008), and right panel: the CH_3OH ($8_{-3,6}$–$9_{-2,8}$) emission zoomed in around the submillimeter continuum peak (redshifted emission is at 61 km s^{-1}, blueshifted emission is at 55 km s^{-1}, levels are 1 to 4 in steps of 0.4 Jy beam^{-1}). These images show the morphology of the various emission tracers with respect to the submillimeter continuum peak and to each other. On large scales, the ^{13}CO (1–0) emission is tracing an outflow in the southwest to northeast direction. On intermediate scales, the ^{13}CO (3–2) emission traces a velocity gradient in the southeast to northwest direction, while on the smallest scales the CH_3OH emission shows a southwest to northeast velocity gradient.

~0.01 pc (~2000 AU; Osorio et al. 1999). We choose this dust temperature because the rotational temperature derived from the CH_3CN fitting above arises from a small region within the beam (see the beam filling factors listed in Table 2). Because the gas and dust are unlikely to be completely thermally coupled, we choose a dust temperature of 100 K to represent the dust emission arising from the larger, and presumably cooler, core region. Therefore, the calculated masses of 8 and 26 $M_\odot$ corresponds to the mass detected within the ~0.01 pc region. If we assume a dust temperature equal to the rotational temperatures derived above, the core masses are both ~4 $M_\odot$.

Bolometric luminosities were recently estimated for these cores from gray-body fits to their IR–submillimeter broadband spectral energy distributions (SEDs; Rathborne et al. 2010). Because the SEDs were generated using single-dish data with angular resolutions of 8″–15″, the values derived from fits to these SEDs correspond to the larger ~1 pc core. Assuming that these cores will give rise to a high-mass star and, hence, a cluster, then they ought to contain numerous low-mass stars in close proximity to the high-mass protostar. However, at the distances to these cores, the 3σ detection limit in the continuum emission corresponds to ~8 $M_\odot$ (assuming a dust temperature of 30 K). Thus, these data are not sufficiently sensitive to detect low-mass protostars and, hence, we are currently unable to determine the multiplicity within these cores. Nevertheless, if these cores contain a high-mass protostar, then it is likely that the derived bolometric luminosity will be dominated by the high-mass star, regardless of the number of undetected low-mass protostars that may be within this larger core.

Assuming that all of the observed bolometric luminosity arises from the single object detected in these high-angular resolution images, we find that their luminosities are $>10^4$ $L_\odot$ consistent with the presence of a high-mass protostar (see Table 1). Moreover, their calculated luminosity-to-mass ratios (L/M) are ~2500 $L_\odot/M_\odot$ and mass column densities, Σ, are ~20–50 g cm^{-2}. These values are consistent with recent theoretical models that predict critical values for $L/M >$ 10 $L_\odot/M_\odot$ and $\Sigma > 1$ g cm^{-2} for the formation of a high-mass star (Krumholz & McKee 2008).

4.3. Kinematics

4.3.1. G034.43+00.24 MM1

Previous single-dish CO (3–2), SiO (2–1), and CS (2–1) observations (17″–55″) show that at least one massive and energetic outflow originates from this core (Sanhueza et al. 2010). The direction of this outflow is consistent with interferometric ^{12}CO (1–0) and SiO (1–0) observations showing a large-scale outflow extending from the southwest to the northeast of the central core (outflow radius of 0.85 pc; Shepherd et al. 2007, Q. Zhang 2010, private communication). This large-scale outflow appears to be orientated perpendicular to an extended (~0.12 pc) ^{13}CO (3–2) structure. The velocity gradient of the ^{13}CO emission and its morphology suggests that the emission may be tracing an extended rotating envelope surrounding the embedded protostar (Rathborne et al. 2008).

While the ^{13}CO emission is resolved out by the interferometer at the angular resolution of our new data, the emission from the many lines of complex molecules can be used to further probe the kinematics within this core. Unresolved at spatial scales of 2″, we find that the line emission from the complex molecules is now resolved in the higher angular resolution data. Figure 4 shows the integrated intensity images for several molecular lines detected toward this core. These transitions were selected as they are bright, appear isolated and are unlikely to be significantly blended. Included in this figure are molecules that typically trace hot cores (CH_3CN, CH_3OH, and CH_3OCH_3), a shock tracer (SO), and their isotopomers ($^{13}CH_3CN$, $^{13}CH_3OH$, and ^{34}SO).

Toward this core we find that the emission from these molecules peak at approximately the same location, which is offset by ~0.25 arcsec from the peak in the submillimeter continuum. This offset could be a result of either temperature or chemical structure surrounding the central protostar. Moreover, extended structure is seen particularly in the SO and CH_3OCH_3

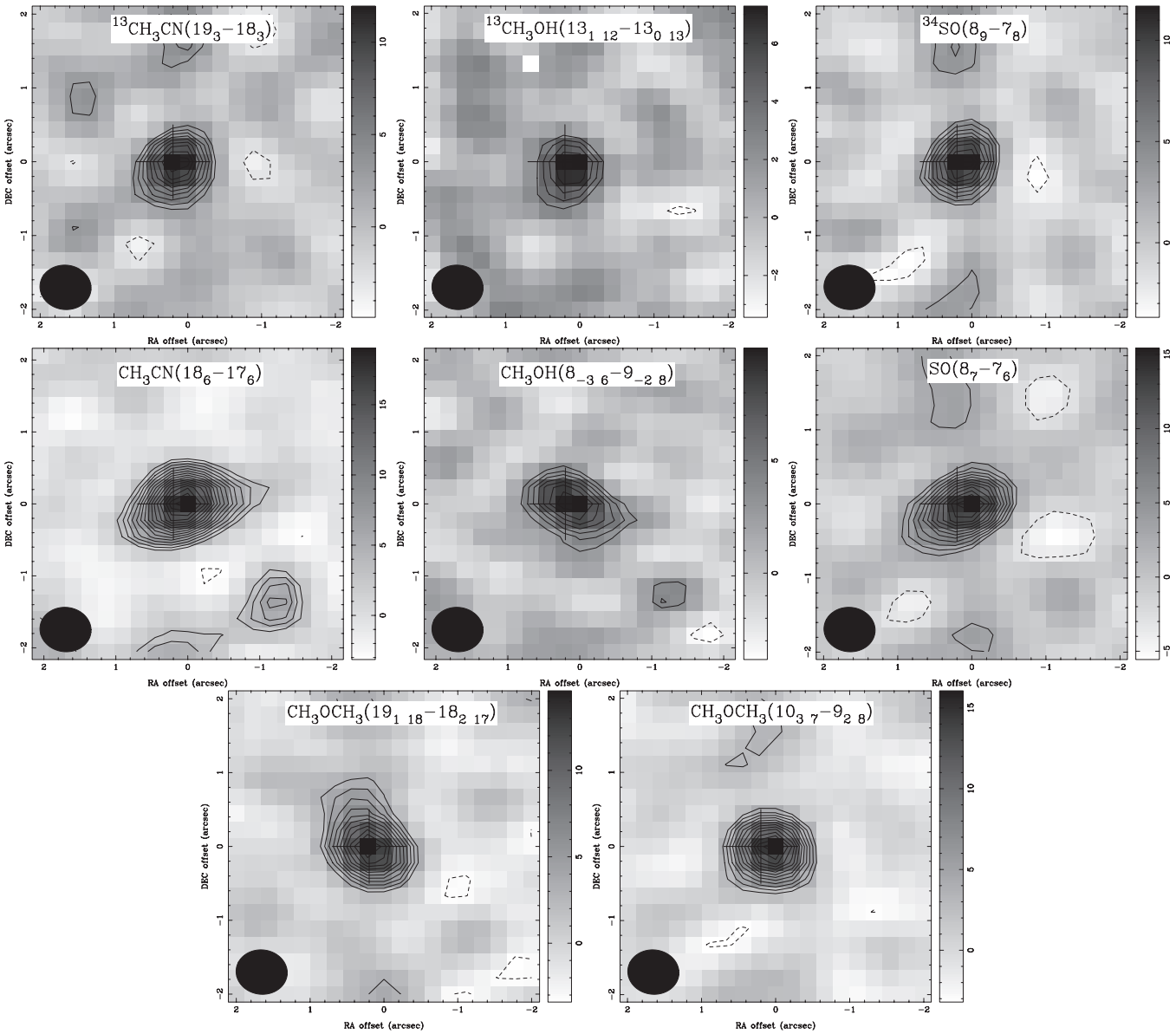

Figure 7. G024.33+00.11 MM1 integrated intensity images for a selection of the bright, unblended lines identified in Figure 3. In all cases the contour levels are -3σ, 3σ to 19σ in steps of 1σ, where σ is 1.0 K km s^{-1}. The cross marks the position of the peak pixel in the continuum emission. The axes on all images are labeled in arcseconds offset from the pointing center of the observations (R.A. 18:35:08.1, decl. −7:35:04, J2000), which was taken from the low-resolution (11″), single-dish continuum image.

lines. Channel maps for these molecular lines (Figure 5) reveal complicated morphologies and, in the CH_3OH emission, a $\sim$5 km s^{-1} velocity gradient. If the emission lines from these complex molecules do indeed arise in the immediate vicinity of a high-mass star, then they can potentially be used to trace a rotating disk: clear evidence for a velocity gradient indicative of rotation exists for at least five other HMCs (see Beltrán et al. 2011 and references therein).

While this velocity gradient is interesting, its direction relative to the larger scale ^{13}CO (3–2) and CO (1–0) structures is puzzling. Figure 6 shows the morphology of the various tracers with respect to the submillimeter continuum peak and to each other. For simplicity we show the large-scale outflow using contours of ^{13}CO (1–0) emission (Shepherd et al. 2007), the intermediate-scale motion using the ^{13}CO (3–2) emission (Rathborne et al. 2008), and the small-scale motions using the CH_3OH emission.

Due to their relative location with hot cores, emission from CH_3CN or CH_3OH is typically used as a disk tracer, with CO tracing any larger scale outflow (e.g., Beltrán et al. 2011). In the case of this HMC, a simple interpretation of an outflow/disk system is problematic. On large scales, the ^{13}CO (1–0) emission is tracing a gradient in the southwest–northeast direction. On intermediate scales, the ^{13}CO (3–2) emission traces a velocity gradient in the southeast–northwest direction, while on the smallest scales the complex molecular emission shows a southwest–northeast velocity gradient. The gas traced by the CO (3–2) lines shows velocity gradient perpendicular to the (1–0) emission, which may be explained by optical depth effects and excitation differences within the central core. The 90 degree change in the direction of the apparent velocity gradient between the ^{13}CO (1–0) and the (3–2) emission makes any interpretation as pure outflow/rotation difficult. Shepherd et al. (2007) do note, however, a second, smaller outflow

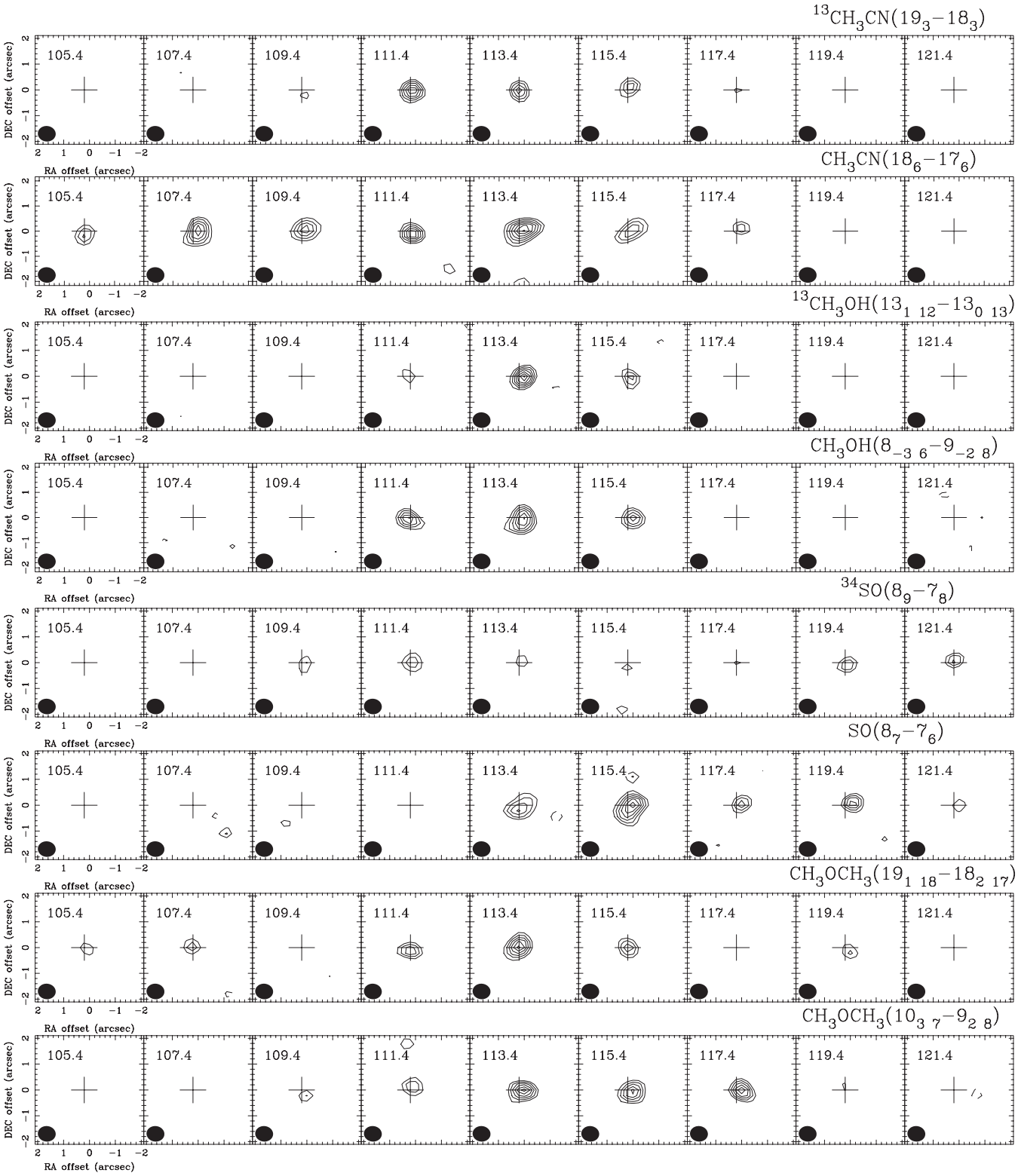

Figure 8. G024.33+00.11 MM1 channel maps of the bright, unblended lines shown in Figure 7. The V_{LSR} for this source is 113.4 km s^{-1}. In all cases the contour levels are -3σ, 3σ to 19σ in steps of 1σ, where σ is 0.17 Jy beam^{-1}. While most lines peak at the V_{LSR} of this core (113 km s^{-1}), it appears that the SO and ^{34}SO peak at different velocities (115 and 111 km s^{-1}), respectively. These differences may arise due to temperature and density gradients within the core.

emanating from this region that is perpendicular to the larger outflow (and, thus, parallel to the ^{13}CO (3–2) emission). While the orientation of this smaller outflow is perpendicular to the large-scale outflow, it is consistent with the outflow/rotating structures seen on the smaller scales. Thus, the structure that we seen on the small scales may correspond to this smaller outflow and not the larger CO (1–0) and SiO (1–0) outflows.

Nevertheless, the densest and presumably hottest gas in the immediate vicinity of the central star (in this case traced by the

CH_3OH emission) is likely to be excited in a disk rather than an outflow. While the velocity gradient apparent in the hot core lines is suggestive of rotation of a disk, the angular separation between the CH_3OH , red, and blue components is $\sim 0\farcs25$, which at the distance to this core corresponds to linear scale of $\sim$1000 AU ($\sim$0.004 pc). This separation and the observed velocity gradient correspond to a dynamical mass for the CH_3CN structure of $\sim 12\ M_\odot$. Because typical accretion disks are seen on spatial scales of a few hundred AU and contain only a few solar masses of material, the CH_3OH emission detected here is still tracing a relatively large, rotating structure and is unlikely to be arising from an accretion disk.

4.3.2. G024.33+00.11 MM1

Similar to G034.43+00.24 MM1 we find that while the continuum emission is unresolved in the higher angular resolution, the molecular line emission is typically resolved and often extended (Figure 7). Moreover, we find that for most molecules, the peak in the integrated intensity emission is slightly offset from the peak in the submillimeter continuum emission (marked with a cross). The exception is for the $CH_3OCH_3(19_{1,18}–18_{2,17})$ emission, which appears coincident with the peak in continuum.

Channel maps for these complex molecules are shown in Figure 8. Interestingly, for this HMC, the channel maps reveal that the emission from different molecular transitions often peak at slightly different velocities. In the majority of cases, the emission peaks at the V_{LSR} of the core ($\sim$113 km s^{-1}). However, the SO emission peaks at 115 km s^{-1}, while the ^{34}SO peaks at 111 km s^{-1}. Detailed modeling is needed to determine whether these differences arise due to temperature and density gradients within the core.

5. CONCLUSIONS

Using the SMA we have obtained high-angular resolution submillimeter continuum images and molecular line spectra toward two cores within IRDCs. These cores are bright ($>$1 Jy), luminous ($>10^4\ L_\odot$), and massive ($10^3\ M_\odot$) and both show "hot core" chemistry. We find that the continuum emission from the cores remains unresolved at spatial scales of $\sim$0.01 pc. From continuum emission toward these small, hot regions, we derive dust masses of $\sim$8 and 26 $M_\odot$.

We find that both cores contain emission from numerous complex molecules and their isotopomers, indicating the presence of "hot cores" within them. Their velocity structures reveal complex kinematics which, for G034.43+00.24 MM1, may trace a rotating structure surrounding the central protostar. Detailed modeling of the numerous molecular lines found within these cores will reveal whether the observed kinematics arise because of temperature or density gradients within the cores. Due to their short lifetimes, HMCs within IRDCs may reveal important clues to the formation of high-mass stars.

This research made use of the myXCLASS program (http://www.astro.uni-koeln.de/projects/schilke/XCLASS), which accesses the CDMS (http://www.cdms.de) and JPL (http://spec.jpl.nasa.gov) molecular data bases. Special thanks go to Peter Schilke for making xclass available to us and especially Sebastien Maret for help installing mySQL and xclass. Thanks to Debra Shepherd for making her ^{12}CO data available to us and to Keping Qiu for help with the CH_3CN fitting. G.G. acknowledges support from CONICYT through projects FONDAP No. 15010003 and BASAL PFB-06. This work was supported in part by the US National Science Foundation by grant AST-0808001.

Facility: SMA.

REFERENCES

Beltrán, M. T., Cesaroni, R., Neri, R., & Codella, C. 2011, A&A, 525, A151
Beuther, H., Schilke, P., Sridharan, T. K., et al. 2002, A&A, 383, 892
Beuther, H., Sridharan, T. K., & Saito, M. 2005, ApJ, 634, L185
Carey, S. J., Clark, F. O., Egan, M. P., et al. 1998, ApJ, 508, 721
Carey, S. J., Feldman, P. A., Redman, R. O., et al. 2000, ApJ, 543, L157
Cesaroni, R., Galli, D., Lodato, G., Walmsley, C. M., & Zhang, Q. 2007, in Protostars and Planets V, ed. B. Reipurth, D. Jewitt, & K. Keil (Tucson, AZ: Univ. Arizona Press), 197
Chambers, E. T., Jackson, J. M., Rathborne, J. M., & Simon, R. 2009, ApJS, 181, 360
Churchwell, E. 2002, ARA&A, 40, 27
Egan, M. P., Shipman, R. F., Price, S. D., et al. 1998, ApJ, 494, L199
Garay, G., Faúndez, S., Mardones, D., et al. 2004, ApJ, 610, 313
Garay, G., & Lizano, S. 1999, PASP, 111, 1049
Hildebrand, R. H. 1983, QJRAS, 24, 267
Ho, P. T. P., Moran, J. M., & Lo, K. Y. 2004, ApJ, 616, L1
Krumholz, M. R., & McKee, C. F. 2008, Nature, 451, 1082
Kurtz, S., Cesaroni, R., Churchwell, E., Hofner, P., & Walmsley, C. M. 2000, Protostars and Planets IV, ed. V. Mannings, A. P. Boss, & S. S. Russell (Tucson, AZ: Univ. Arizona Press), 299
Lis, D. C., & Carlstrom, J. E. 1994, ApJ, 424, 189
Mookerjea, B., Casper, E., Mundy, L. G., & Looney, L. W. 2007, ApJ, 659, 447
Olmi, L., Cesaroni, R., Neri, R., & Walmsley, C. M. 1996, A&A, 315, 565
Ormel, C. W., Shipman, R. F., Ossenkopf, V., & Helmich, F. P. 2005, A&A, 439, 613
Osorio, M., Lizano, S., & D'Alessio, P. 1999, ApJ, 525, 808
Ossenkopf, V., & Henning, T. 1994, A&A, 291, 943
Pillai, T., Wyrowski, F., Menten, K. M., & Krügel, E. 2006, A&A, 447, 929
Qiu, K., & Zhang, Q. 2009, ApJ, 702, L66
Rathborne, J. M., Jackson, J. M., Chambers, E. T., et al. 2005, ApJ, 630, L181
Rathborne, J. M., Jackson, J. M., Chambers, E. T., et al. 2010, ApJ, 715, 310
Rathborne, J. M., Jackson, J. M., & Simon, R. 2006, ApJ, 641, 389
Rathborne, J. M., Jackson, J. M., Zhang, Q., & Simon, R. 2008, ApJ, 689, 1141
Rathborne, J. M., Simon, R., & Jackson, J. M. 2007, ApJ, 662, 1082
Sanhueza, P., Garay, G., Bronfman, L., et al. 2010, ApJ, 715, 18
Shepherd, D. S., Nürnberger, D. E. A., & Bronfman, L. 2004, ApJ, 602, 850
Shepherd, D. S., Povich, M. S., Whitney, B. A., et al. 2007, ApJ, 669, 464
Simon, R., Rathborne, J. M., Shah, R. Y., Jackson, J. M., & Chambers, E. T. 2006, ApJ, 653, 1325
Solomon, P. M., Jefferts, K. B., Penzias, A. A., & Wilson, R. W. 1971, ApJ, 168, L107
Wang, Y., Zhang, Q., Rathborne, J. M., Jackson, J., & Wu, Y. 2006, ApJ, 651, L125
Zhang, Q. 2005, in IAU Symp. 227, Massive Star Birth: A Crossroads of Astrophysics, ed. R. Cesaroni, M. Felli, E. Churchwell, & M. Walmsley (Cambridge: Cambridge Univ. Press), 135
Zhang, Q., Hunter, T. R., Brand, J., et al. 2001, ApJ, 552, L167
Zhang, Q., Hunter, T. R., Brand, J., et al. 2005, ApJ, 625, 864